energies

MDPI

Article

Numerical Simulation of Vertical Well Depressurization with Different Deployments of Radial Laterals in Class 1-Type Hydrate Reservoir

Tinghui Wan [1,2], Miao Yu [1,2,*], Hongfeng Lu [1,2], Zongheng Chen [1,2], Zhanzhao Li [1,2], Lieyu Tian [1,2], Keliang Li [1,2], Ning Huang [1,2] and Jingli Wang [1,2,*]

[1] Guangzhou Marine Geology Survey, China Geological Survey, Ministry of Natural Resources, Guangzhou 511458, China; atomion@126.com (T.W.); luhongfeng@hydz.cn (H.L.); czhgs@126.com (Z.C.); 13650780173@163.com (Z.L.); tianlieyu23@163.com (L.T.); likeliang@mail.cgs.gov.cn (K.L.); hnabc2003@163.com (N.H.)

[2] National Engineering Research Center for Gas Hydrate Exploration and Development, Guangzhou 511458, China

* Correspondence: yumiao104@163.com (M.Y.); wjl06012527@126.com (J.W.)

Abstract: Gas production efficiency is a key indicator in the commercial development of natural gas hydrates (NGHs). Based on the data from the first natural gas hydrate field test production in the Shenhu Sea area of China, the gas production capability of Class 1-type hydrate reservoirs was numerically evaluated by vertical well depressurization with different deployment schemes for radial laterals. The results showed that the radial laterals can effectively improve production efficiency and that the radial laterals deployed at the three-phase layer (TPL) have the best production performance. Compared with the single vertical well production, the completion length of the radial laterals is 150 m with a radius of 0.05 m, and the production pressure difference is set to 6 MPa. The cumulative gas production V_g reaches up to 594.10 $\times$ 10^4 ST m^3, increased by about 208.53% after 360 days of production, which provides a reference for the development of natural gas hydrates with radial jet drilling (RJD) technology.

Keywords: natural gas hydrate; radial jet drilling; radial laterals; numerical simulation; TOUGH+HYDRATE

Citation: Wan, T.; Yu, M.; Lu, H.; Chen, Z.; Li, Z.; Tian, L.; Li, K.; Huang, N.; Wang, J. Numerical Simulation of Vertical Well Depressurization with Different Deployments of Radial Laterals in Class 1-Type Hydrate Reservoir. *Energies* **2024**, *17*, 1139. https://doi.org/10.3390/en17051139

Academic Editor: Hossein Hamidi

Received: 1 February 2024
Revised: 19 February 2024
Accepted: 23 February 2024
Published: 28 February 2024

1. Introduction

Natural gas hydrates (NGHs) are widely present in permafrost regions and deep-sea sediments. According to research results, there is approximately 3.0 $\times$ 10^{15} to 2.5 $\times$ 10^{18} ST m^3 of CH_4 trapped in NGH reservoirs around the world [1–3]. Consequently, NGHs have been suggested as potential substitutes for fossil fuels [4]. At present, depressurization has been demonstrated as the most effective method for marine gas hydrate exploitation by recent offshore test production in China's Shenhu Sea area and Japan's Nankai Trough [5–8]. However, the daily average gas production of this test production is significantly lower than that of the commercial development standard of 5 $\times$ 10^5 m^3/d [1]. Therefore, improving the gas production efficiency becomes a critical challenge to the commercial development of NGHs. Radial jet drilling (RJD) is an unconventional drilling technique, which has been widely used for lateral drilling in the petroleum industry [9–13]. RJD technology has the advantages of technical feasibility and low costs. Therefore, it is considered an important production enhancement technology in the development of NGHs and has received a lot of attention in recent years. For example, Li et al. (2020) innovatively proposed radial jet drilling and screen completion combined with the depressurization method to exploit hydrates. The entire process flow, jet rock breaking drilling capabilities, jet extension length limit, and borehole trajectory monitoring and control are all covered [14]. Zhang et al. used the numerical method to study the performance of radial well depressurization in

exploitation hydrates and found that radial wells can significantly improve gas recovery rates in the early stages of production. The recovery rate of hydrates is linearly related to the radial lateral length. Under the same pressure drop conditions, the cumulative gas production of radial well is three times that of the vertical well [15,16]. Zhang et al. (2022) analyzed the water jet erosion process of NGH- and hydrate-bearing sediments (HBS). The results show that there are specific shapes for NGH and HBS [17]. In a different study, Zhang et al. (2022) used vertical and radial wells to extract hydrate samples rich in water, and the experiment results showed that compared with vertical well production, the cumulative gas production and cumulative water production of the radial wells increased by 20.16% and 38.98%, respectively [18]. Hui et al. simulated the hydrate decomposition process by fracturing of the radial horizontal well. Results indicate that fractures can effectively improve the production efficiency of NGH. When the total fracture length is the same, productivity can be improved by increasing the number of fractures. Horizontal and vertical fractures boosted gas production by 306% and 550%, respectively [19,20]. The above research work has substantially promoted the application of RJD technology in hydrate exploitation. Nevertheless, previous studies mainly focused on Class 3-type hydrate reservoirs, and the effect of deploying different radial laterals on vertical well depressurization in Class 1-type hydrate reservoirs it is still unclear. Herein, a numerical model was established, and the production behaviors of vertical wells deployed with different radial laterals were systematically investigated. Our results provide a reference for the development of NGHs with RJD technology.

2. Radial Jet Drilling

Figure 1 depicts the schematic diagram of RJD and NGH production by radial wells. The first step is to complete vertical drilling and casing for cementing. The second step is to use the coiled tubing to carry special tools and drill a hole with a diameter of 22 mm on the target layer casing. The third step is to use the coiled tubing hydraulic jetting system (with a slotted liner) to perform hydraulic jetting drilling in the formation with strong jetting and self-propulsion capabilities. The last step is to separate the coiled tubing and the slotted liner. According to previous literature reports, the latest radial jet drilling assembly can jet radial laterals with a length of up to 100 m [14–16,21–23].

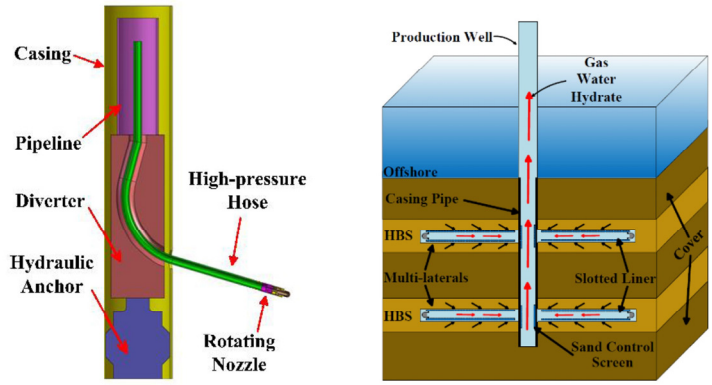

Figure 1. Schematic diagram of radial jet drilling (RJD) (**left**) and natural gas hydrate production by radial laterals (**right**) (from Zhang et al., 2022) [17].

3. Methodology

3.1. Geological Background

The SHSC4 well is between the Xisha Trough and the Dongsha Islands (Figure 2). The water depth in this location is around 1266 m, the seabed temperature is around 3 °C, and the gradient of geothermal is 43.653 °C/km [7]. It has been selected as China's first offshore NGH field trial target station [24]. The NGH reservoir system belongs to a Class 1-type hydrate reservoir, which can be divided into three layers based on the on-site data. The upper part is the gas hydrate-bearing layer (GHBL), which is rich in hydrate and

water, with a burial depth of 201–236 mbsf and a thickness of 35 m. The middle part is the three-phase layer (TPL), which contains hydrates, high saturation free gas, and water, with a burial depth of 236–251 mbsf and a thickness of 15 m. The free gas layer (FGL) is composed of low saturation free gas and water, with a burial depth of 251–278 mbsf and a thickness of 27 m [7].

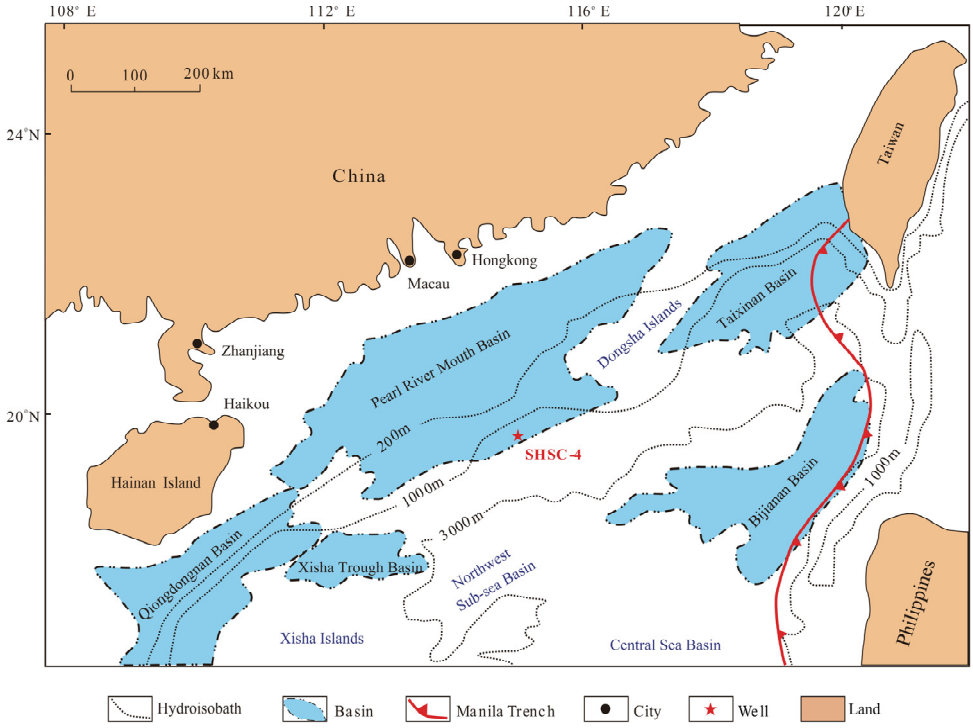

Figure 2. SHSC4 well location diagram (from Li et al., 2018) [7].

3.2. Simulation Code

TOUGH+HYDRATE V1.0, as the professional NGH simulation code, includes dynamic and equilibrium models, comprehensively considers various phase states and components, and can simulate hydrate dissociation methods such as depressurization and thermal stimulation [25]. After experimental and on-site testing comparisons, the effectiveness of this code has been widely recognized [26,27]. This work adopted the parallel version of this code and employed a thermodynamic equilibrium model to simulate long-term natural gas production [28,29]. The following assumptions were made: (1) Darcy's law is effective in the model; (2) the movement of geological media is neglected; (3) mechanical dispersion of dissolved gases and inhibitors is ignored; (4) the aqueous phase is not allowed to disappear when salts are present; (5) dissolved inhibitors have no effect on the thermophysical properties of the aqueous phase; and (6) the inhibitor is a non-volatile component. The control equations of multiphase flow, thermal convection, and conduction processes are given as follows [25]:

1. Phases and components

Phase state (β) comprises solid hydrates (H), ice (I), water (A), and gas (G); Components (κ) include hydrates (h), inhibitors (i), water (w), and methane gas (m).

2. Mass balance

The flow control equation for multi-component fluid mixtures based on mass balance is as follows:

$$\frac{d}{dt}\int_{V_n} M^{\kappa} dV = \int_{\Gamma_n} F^{\kappa} \cdot n d\Gamma + \int_{V_n} q^{\kappa} dV \quad (1)$$

Here, M^{κ} is the mass accumulation, F^{κ} is the flux, and q^{κ} is the source/sink ratio.

The mass accumulation term M^κ is defined as follows:

$$M^\kappa = \sum_{\beta=A,G,H,I} \varphi S_\beta \rho_\beta X_\beta^\kappa \tag{2}$$

The mass flux term F^κ is determined by the aqueous and gaseous phases:

$$F^\kappa = \sum_{\beta=A,G} \left(F_\beta^\kappa + J_\beta^\kappa \right) \tag{3}$$

Based on the multiphase Darcy's law, F_A^κ is defined as follows:

$$F_A^\kappa = X_A^\kappa F_A, F_A = -k \frac{k_{rA} \rho_A}{\mu_A} (\nabla P_A - \rho_A g) \tag{4}$$

Based on the Klinkenberg function, F_A^κ is determined by the following equation:

$$F_G^\kappa = X_G^\kappa F_G, F_G = -k \left(1 + \frac{b}{P_G} \right) \frac{k_{rG} \rho_G}{\mu_G} (\nabla P_G - \rho_G g) \tag{5}$$

Based on the Fick's law, the diffusive mass flux of component κ ($\kappa = m, i$) is defined as follows:

$$J_\beta^\kappa = -\varphi S_\beta \tau_\beta D_\beta^\kappa \rho_\beta \nabla X_\beta^\kappa \tag{6}$$

3. Energy balance

The heat flow control equation based on energy balance is as follows:

$$\frac{d}{dt} \int_{V_n} M^\theta dV = \int_{\Gamma_n} F^\theta \cdot n d\Gamma + \int_{V_n} q^\theta dV \tag{7}$$

Here, θ is the heat component, M^θ, F^θ, and q^θ are the heat accumulation, flux, and source/sink ratio, respectively. The heat accumulation term M^θ is determined by the rock matrix and all the phases as follows:

$$M^\theta = (1 - \varphi) \rho_R C_R T + \sum_{\beta=A,G,H,I} \varphi S_\beta \rho_\beta U_\beta + Q_d \tag{8}$$

The heat flux term F^θ is determined by the conduction and advection as follows:

$$F^\theta = -\lambda_\theta \nabla T + \sum_{\beta=A,G} h_\beta F_\beta \tag{9}$$

Reaction heat Q_d of hydrate dissociation is defined as follows:

$$Q_d = \begin{cases} \Delta(\varphi \rho_H S_H \Delta U_H) \; for \; equilibrium \; dissociation \\ \Delta Q_H \cdot U_H \; for \; kinetic \; dissociation \end{cases} \tag{10}$$

4. Phase changes

The Phase changes control equation is as follows:

$$P = exp(e_1 + \frac{e_2}{T}) \tag{11}$$

Here, P is the phase equilibrium pressure (Kpa); T is the phase equilibrium temperature (K), and e_1 and e_2 are the regression parameters.

The parameter values are as follows:

$$e_1 = \begin{cases} 38.980 \\ 14.717 \end{cases}, e_2 = \begin{cases} -8533.80 \\ -1886.79 \end{cases}, (T = T_C + 273.15) \tag{12}$$

$$\text{For} \begin{cases} 0\ ^{\circ}\text{C} \le T_c \le 25\ ^{\circ}\text{C} \\ -25\ ^{\circ}\text{C} \le T_c \le 0\ ^{\circ}\text{C} \end{cases} \quad (13)$$

5. Stress

The Stress control equation is as follows:

$$\varphi_a = F_{PT}\varphi_{rr}(1 - S_s) \quad (14)$$

Here, φ_a is the available porosity for fluids, φ_{rr} is the relative magnitude of φ, S_s is the solid saturation. F_{PT} is a porosity adjustment factor that accounts for the effects of pressure and temperature on porosity, which can be estimated from the following equation:

$$F_{PT} \approx 1 + \alpha_P \Delta P + \alpha_T \Delta T \quad (15)$$

Here, α_P and α_T are the pore compressibility and thermal expansivity, respectively.

3.3. Model Construction and Case Design

Based on the on-site data, a large-scale numerical model was created (Figure 3a). The size of the simulation area is 400 × 400 × 117 m in (x, y, z). Previous research has shown that setting the overburden (OB) and underburden (UB) thicknesses to 20 m is enough to eliminate the border effects [30]. As indicated in Figure 3a, the reservoir was further separated into three sublayers: the GHBL, TPL, and FGL, with thicknesses of 35 m, 15 m, and 27 m, respectively [7,31]. To investigate the impacts of radial laterals with different deployments on gas production, a total of eight simulation cases were established, as shown in Figure 3c. The open hole completion length of the vertical well is 70 m, with a radius of 0.1 m. The radial laterals are open hole completion with a radius of 0.05 m, and the parameters are listed in Table 1.

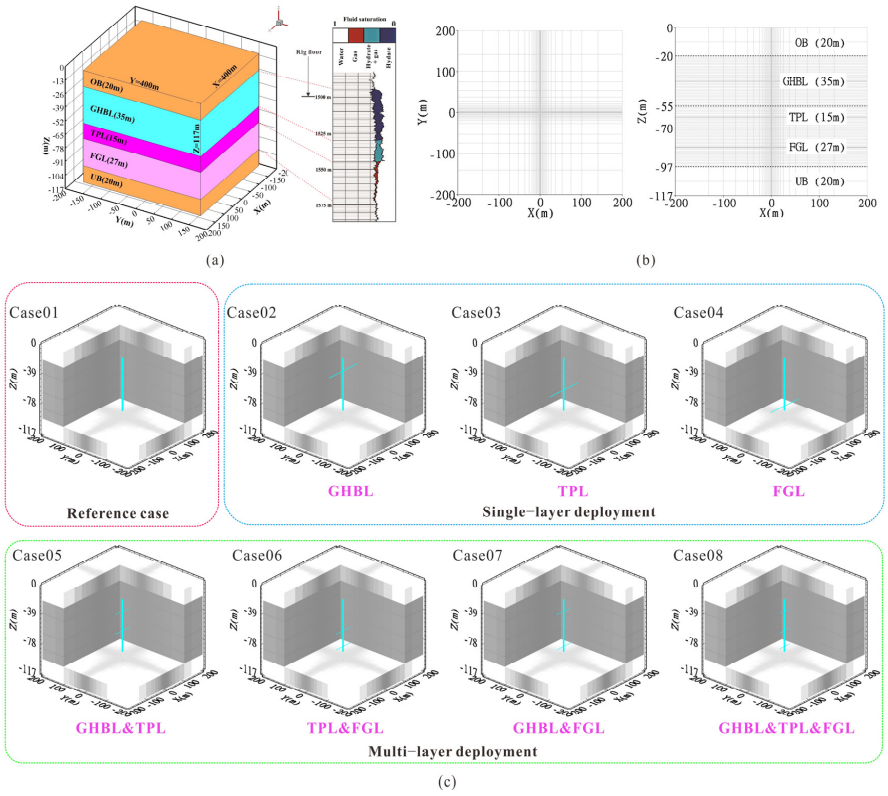

Figure 3. Model schematic diagram and cases design: (**a**) Geological model & Logging curve of SHSC-4 well. (**b**) Model mesh. (**c**) Vertical well with different radial laterals deployment.

Table 1. Parameters of radial laterals in simulation cases.

Groups	Case	Main Parameters of Radial Laterals			
		n	*l* (m)	*L* (m)	Deployment Location
Single vertical well	Case 01	-	-	-	-
Single-layer deployment	Case 02	2	75	150	GHBL
	Case 03	2	75	150	TPL
	Case 04	2	75	150	FGL
Multi-layer deployment	Case 05	4	37.5	150	GHBL & TPL
	Case 06	4	37.5	150	TPL & FGL
	Case 07	4	37.5	150	GHBL & FGL
	Case 08	6	25	150	GHBL & TPL & FGL

The x–y plane domain was discretized into 1361 grids and then extruded into 3D discretized grids along the z-axis, with a total of 126,573 grids, as shown in Figure 3b. Hydrate dissociation is mainly distributed around the wellbore, the local grid refinement is beneficial for evaluating changes in reservoir characteristics, and the minimum grid sizes used in the model are x = 0.05 m, y = 0.05 m, and z = 0.05 m.

3.4. Initial and Boundary Conditions

Initial conditions can be calculated by the self-balancing function of the code, as shown in Figure 4 [32–34]. The Dirichlet boundary conditions are established by setting the reservoir model's top and bottom pressure and temperature to fixed values, as well as the boundary conditions around the model [35]. The wellbore grids were given a fixed pressure difference of 6 MPa and ignored the pressure loss along the wellbore. According to the Navier–Stokes equation theory of fluid mechanics, the wellbore is considered a "pseudo-porous medium" in the model, and the fluid inside the wellbore follows Darcy flow [36]. This "pseudo-porous medium" has a porosity of 1, permeability of 1×10^4 μm^2, capillary force of 0, relative permeability that is a linear function of the saturation of each phase, and very low residual gas saturation [36].

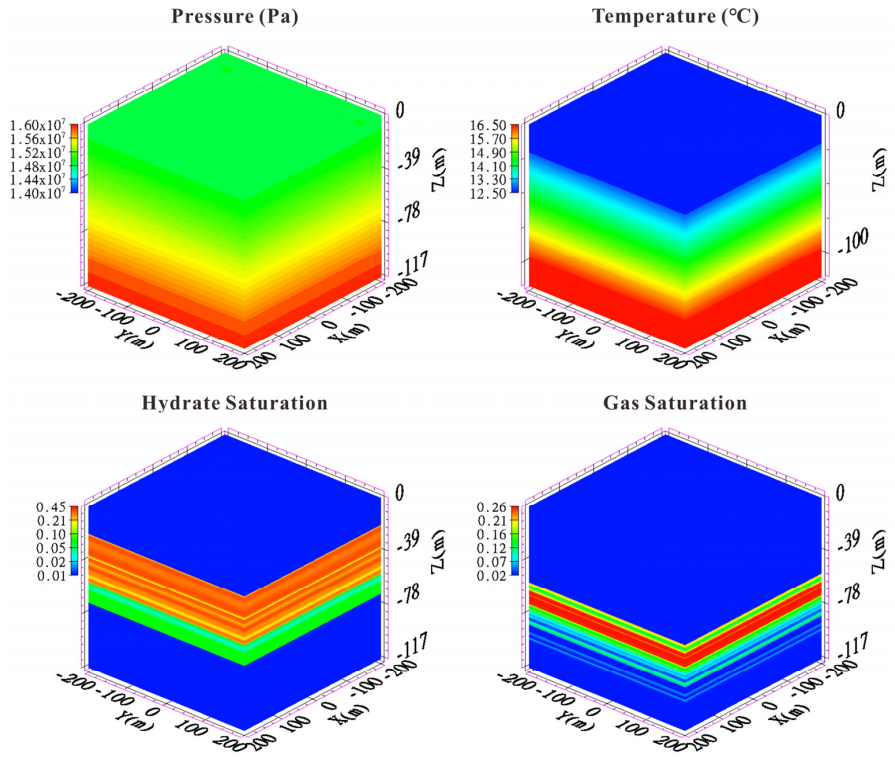

Figure 4. Model's initial conditions.

The average permeability of GHBL, TPL, and FGL was set to 2.9, 1.5, and 7.4 mD respectively, based on the logging curve, extracted saturation data of these three layers for the establishment of the numerical model [7,37]. The permeability and porosity of the OB and UB layers in this work were assumed to be 2.0 mD and 0.3, respectively. The properties of the reservoir model and the simulation parameters are listed in Table 2.

Table 2. Main physical properties of numerical models.

Parameter	Value & Unit
OB and UB thickness	20 m
GHBL thickness	35 m
TPL thickness	15 m
FGL thickness	27 m
OB and UB permeability	2.0 mD
GHBL permeability	2.9 mD
TPL permeability	1.5 mD
FGL permeability	7.4 mD
Vertical wellbore length	70 m, in accordance with the model's −21 m to −91 m
Vertical wellbore radius	0.1 m
Radial laterals radius [10]	50 mm
Salinity	3.5%
GHBL and TPL hydrate saturation	Reference from logging curve (Figure 3a)
FGL gas saturation	Reference from logging curve (Figure 3a)
OB and UB porosity	0.30
GHBL porosity	0.35
TPL porosity	0.33
FGL porosity	0.32
Grain density	2600 kg/m^3
Geothermal gradient	43.653 °C/km
Grain specific heat	1000 $J{\cdot}kg^{-1}{\cdot}K^{-1}$
Gas composition	100% CH_4
Dry thermal conductivity	1.0 $W{\cdot}m^{-1}{\cdot}K^{-1}$
Wet thermal conductivity	3.1 $W{\cdot}m^{-1}{\cdot}K^{-1}$
Capillary pressure model [37–39]	$P_{cap} = -P_0\left[(S^*)^{-1/\lambda} - 1\right]^{1-\lambda}$, $S^* = \frac{(S_A - S_{irA})}{(S_{mxA} - S_{irA})}$
S_{mxA}	1
λ	0.45
P_0	10^4 Pa
Relative permeability model [37–39]	$K_{rA} = [(S_A - S_{irA})/(1 - S_{irA})]^{nA}$, $K_{rG} = [(S_G - S_{irG})/(1 - S_{irA})]^{nG}$
n_A	3.5
n_G	2.5
S_{irG}	0.03
S_{irA}	0.30

3.5. Model Validation

The applicability of the numerical mode constructed in this work is validated by on-site data. The numerical mode includes a vertical well with a completion section of 201 to 271 mbsf (following the model's −21 to −91 m), a length of 70 m, and a production difference of 3 MPa [40]. Figure 5 depicts the fitting result during the first field trial in the Shenhu area in 2017. Based on the gas production fitting results, it is confirmed that the model can be used for subsequent work.

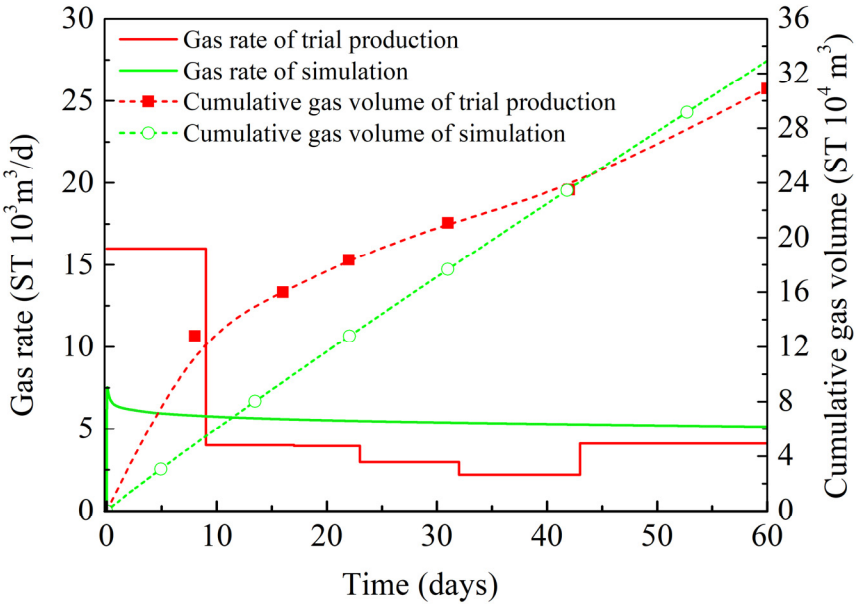

Figure 5. On-site gas production fitting.

4. Results and Discussion

4.1. Single-Layer Deployment

4.1.1. Gas and Water Production

Figure 6a,b depict the evolution of the gas production rate (Q_g) and cumulative gas production (V_g) with single-layer deployment of radial laterals in a vertical well under a production pressure difference of 6 MPa within 360 days. Under the driving force of a large production pressure difference, when the radial laterals were deployed at the GHBL, TPL, and FGL respectively, their gas production rates Q_g reached their peak in the initial stage but gradually decreased in the later stage due to the dual effects of weakened driving force and secondary hydration generation. After 360 days of production, the cumulative gas production V_g were 314.80 $\times$ 10^4, 594.10 $\times$ 10^4, and 427.50 $\times$ 10^4 ST m^3, compared to the single vertical well, increased by 110.49%, 208.53%, and 150.05%, respectively. This indicates that using RJD technology to construct radial laterals in vertical wella can significantly increase productivity due to the increase in the drainage area of the entire system.

The slow increase in gas production rate in the early stage is due to the presence of solid hydrates in the GHBL resulting in a low initial effective permeability of the reservoir. As the solid hydrates around the wellbore gradually decompose, the permeability of the reservoir around the wellbore also increases, resulting in effective pressure propagation and increased gas production from hydrate decomposition within 170 days, while the sudden increase in gas production rate at 170 days is mainly due to the free gas from the TPL beginning to reach and flow into the radial lateral wellbores. In the later stage, it is gradually decreasing due to the dual effects of weakened driving force and secondary formation of hydrates. When the radial laterals are deployed at the TPL, the gas production rate and cumulative gas production are the highest, because they can simultaneously recover high saturation free gas and hydrate decomposition gas in the TPL. When the radial laterals are deployed at the FGL, a sudden increase in the gas production rate curve can be observed at 20 days. This is because the high saturation free gas from the TPL begins to reach and flow into the radial lateral wellbores. Similarly, due to the weak driving force and secondary hydrate formation, there is a gradual decreasing trend in the later stage.

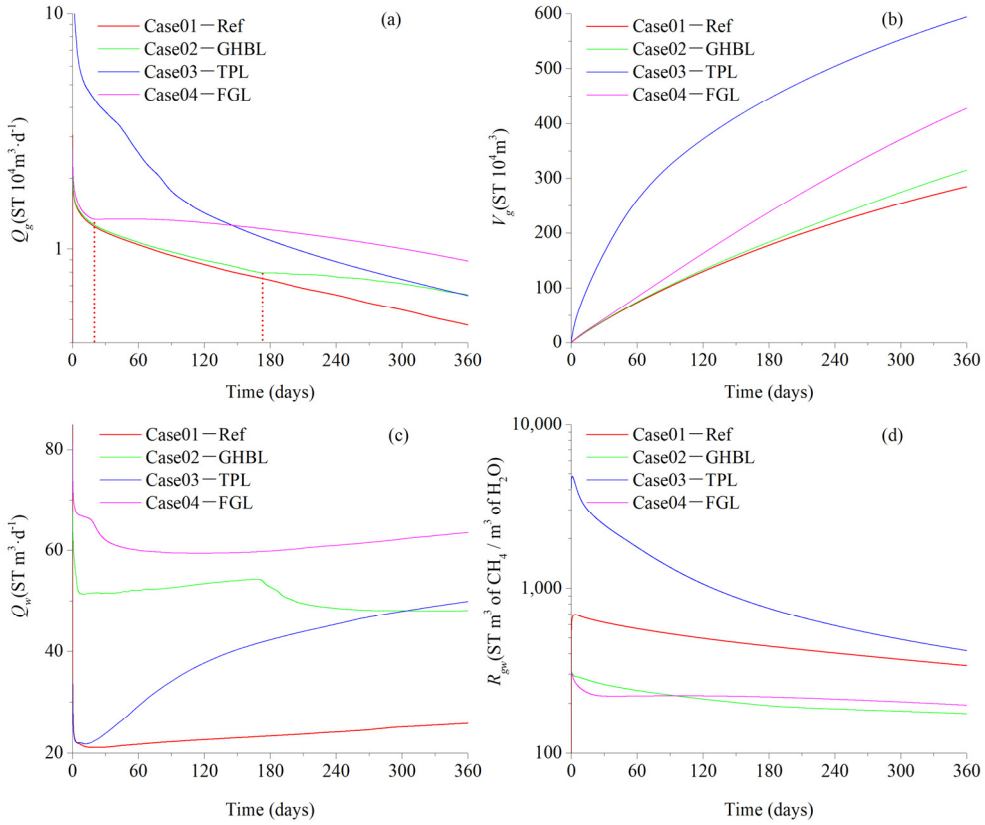

Figure 6. Gas and water production performances of single-layer deployment of radial laterals: (**a**) Gas production rate Q_g. (**b**) cumulative gas production V_g. (**c**) Water production rate Q_w. (**d**) gas to water ratio R_{gw}.

The evolution of the water production rate (Q_w) and the gas to water ratio (R_{gw}), which correspond to gas production behavior, are shown in Figure 6c,d. When the radial laterals are deployed at the GHBL and FGL, their water production rate Q_w is higher, mainly because the original average water saturation of the GHBL and FGL is higher, at around 66% and 93%, respectively. Moreover, when the radial laterals are deployed at the GHBL, the water production rate Q_w shows a sudden decrease at 170 days due to the impacts of low saturation free gas flowing into the radial lateral wellbores. When the radial laterals are deployed at the TPL, the water production rate Q_w is relatively low because most of the water in this layer is bound water. The R_{gw} (ST m^3 of CH_4/ST m^3 of water) is a critical index for evaluating gas production efficiency, where a higher R_{gw} indicates that gas production is economically feasible. When the radial laterals were deployed at GHBL, TPL, and FGL respectively, their R_{gw} was stable at around 170, 400, and 190 after 360 days of production. Table 3 shows the productivity for the aforementioned single-layer deployment cases.

Table 3. Productivity of single-layer deployment of radial laterals.

Case	Deployment Location	Wellbore Contact Area (m^2)	Average Q_g (10^4 m^3/d)	V_g (10^4 m^3)	Compared to the Reference Case
Case 03	GHBL	91.10	1.65	594.10	208.53%
Case 04	TPL	91.10	1.19	427.50	150.05%
Case 02	FGL	91.10	0.87	314.80	110.49%
Case 01 (reference case)	-	43.98	0.79	284.90	100.00%

4.1.2. Spatial Distribution of Physical Properties

As shown in the pressure distribution field diagram Figure 7a, the pressure drop areas between the main wellbore and radial laterals are larger and the pressure gradient between the main wellbore and radial lateral gradually increases from the bottom to the top of the reservoir. This phenomenon occurs due to the dual effects of pressure superposition and gas expansion on the lower gas-bearing layer. In the temperature and hydrate saturation distribution field diagram (Figure 7b,c), it can be observed that except in the case with the radial laterals deployed in the middle of the TPL, other cases have formed obvious relatively low-temperature areas and high saturation secondary hydrates in the reservoir near the wellbore located in the TPL. This is because most of the gas production comes from the high saturation free gas of the TPL. These cases only have a 15 m vertical wellbore connected to the reservoir in the TPL and the total connection area is only approximately 9.5 m^2. Under such a small connection area, a large amount of free gas flows into the wellbore and causes an extremely strong Joule–Thomson effect in the reservoir near the wellbore located in the TPL. Unlike the above cases, when the radial laterals were deployed in the middle of the TPL, except the 15 m vertical wellbore connected to the reservoir in the TPL, there are also radial laterals connected to the reservoir. The total connection area in the TPL is approximately 56.6 m^2, which is about six times that of other cases. Due to the large connection area, the Joule–Thomson effect is weak. As shown in Figure 7d, the gas saturation distribution field diagram corresponds to the gas production. When the radial laterals were deployed in the TPL, the degree of free gas recovery in the reservoir was higher and its gas production rate was also the best. Under the influence of production pressure difference, when the radial laterals were deployed in the GHBL, it can be observed that low-saturation free gas migrated towards the radial laterals. When the radial laterals were deployed in the FGL, high-saturation free gas can be observed migrating towards the radial laterals.

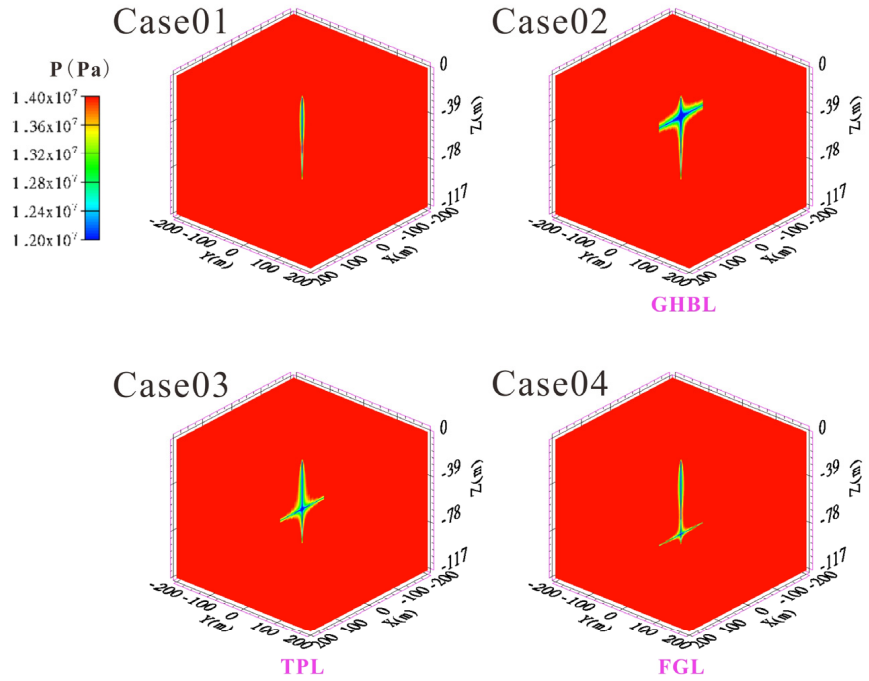

(a)

Figure 7. *Cont.*

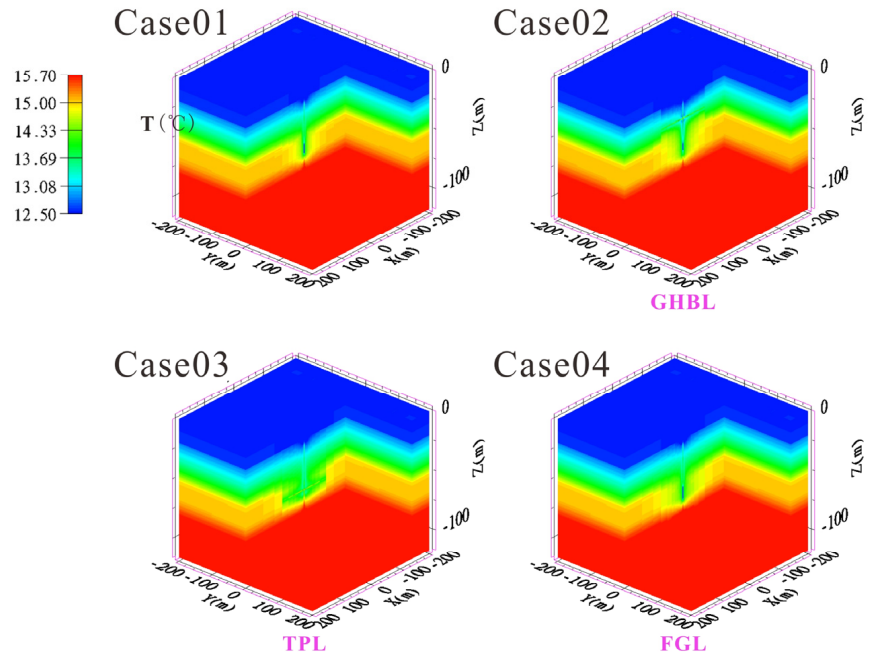

(b)

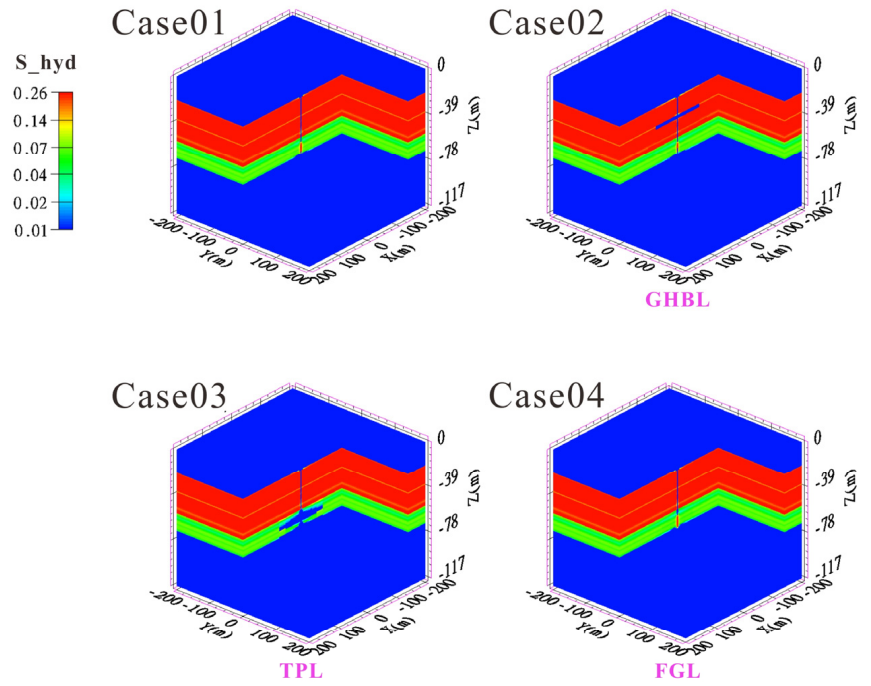

(c)

Figure 7. *Cont*.

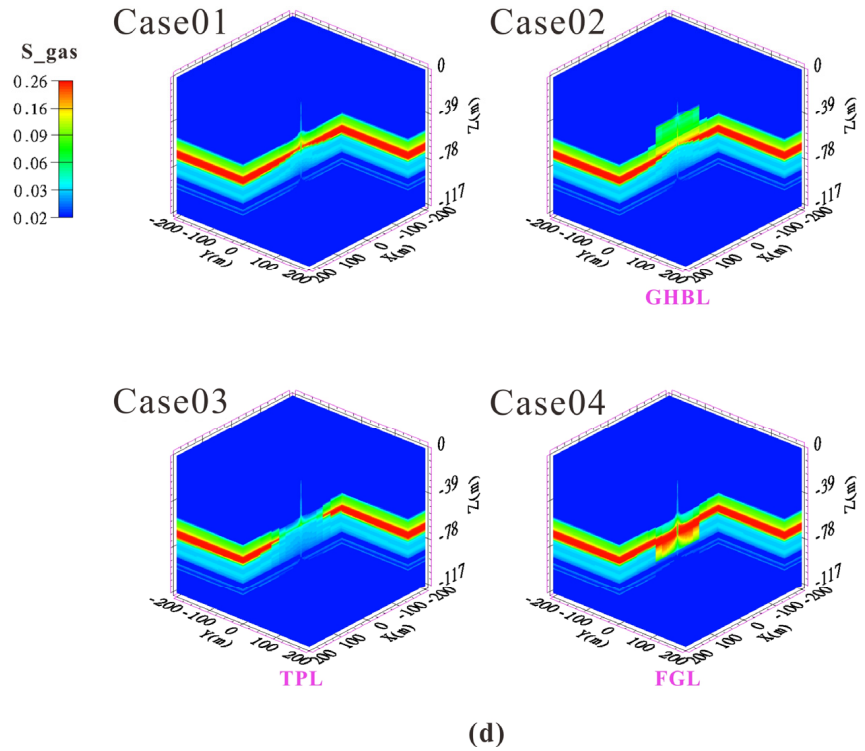

Figure 7. Spatial distribution diagrams of pressure, temperature, and saturation of single-layer deployment of radial laterals: (**a**) Pressure. (**b**) Temperature. (**c**) Hydrate saturation. (**d**) Gas saturation.

4.2. Multi-Layer Deployment

4.2.1. Gas and Water Production

Figure 8a,b depict the evolution of Q_g and V_g with multi-layer deployment of radial laterals in vertical wells under a production pressure difference of 6 MPa within 360 days. When the radial laterals were deployed in the GHBL & TPL, TPL & FGL, GHBL & FGL, and GHBL & TPL & FGL respectively, their Q_g reached its peak in the early stage and decreased later due to weakened driving force and secondary hydrate formation. The Q_g curve shape of the different multi-layer deployments of radial laterals above was a superposition of the Q_g curve shape of the corresponding single-layer radial-lateral deployment. After 360 days of production, the V_g were 454.50×10^4, 503.30×10^4, 377.60×10^4, and 459.00×10^4 ST m^3; compared to the single vertical well, values increased by 159.53%, 176.66%, 132.54%, and 161.11%, respectively. The evolution of the Q_w and the R_{gw}, which correspond to gas production behavior, are shown in Figure 8c,d. When the radial laterals were deployed at the GHBL & TPL, TPL & FGL, GHBL & FGL, and GHBL & TPL & FGL, respectively, their R_{gw} was stable at around 290, 270, 180, and 250 after 360 days of production. Table 4 shows the productivity for the aforementioned multi-layer deployment cases.

4.2.2. Spatial Distribution of Physical Properties

As shown in the pressure distribution field diagram in Figure 9a, when the radial laterals were deployed in multiple layers, the pressure drop areas between the main wellbore and radial laterals were larger and the pressure gradient between the main wellbore and radial laterals located in the upper part was greater, while the one located in the lower part as smaller. The dual effects of pressure superposition and gas expansion on the lower gas-bearing layer cause this phenomenon. As shown in temperature and hydrate saturation distribution field diagram (Figure 9b,c), when the radial laterals were deployed at GHBL and FGL simultaneously, the main wellbore located in the TPL section generated obvious relatively low-temperature areas and secondary hydrates, which is due to the small connection area between the main wellbore and the reservoir in the TPL

section (approximately 9.4 m^2). A large amount of high-saturation free gas enters the wellbore here and causes the strong Joule–Thomson effect. However, other cases have the radial laterals deployed in the TPL, and their main wellbore in the TPL section has a larger connection area with the reservoir (approximately 33 m^2), resulting in a relatively smaller Joule–Thomson effect and no formation of relatively low-temperature areas. Some secondary hydrates were generated at the root of the radial laterals located in the TPL section, as shown in the gas saturation field diagram (Figure 9d). Under the effect of production pressure difference, the free gas located in the TPL migrates towards the upper and lower radial laterals, respectively, which corresponds to the gas production situation, and the degree of recovery of high saturation free gas is relatively low.

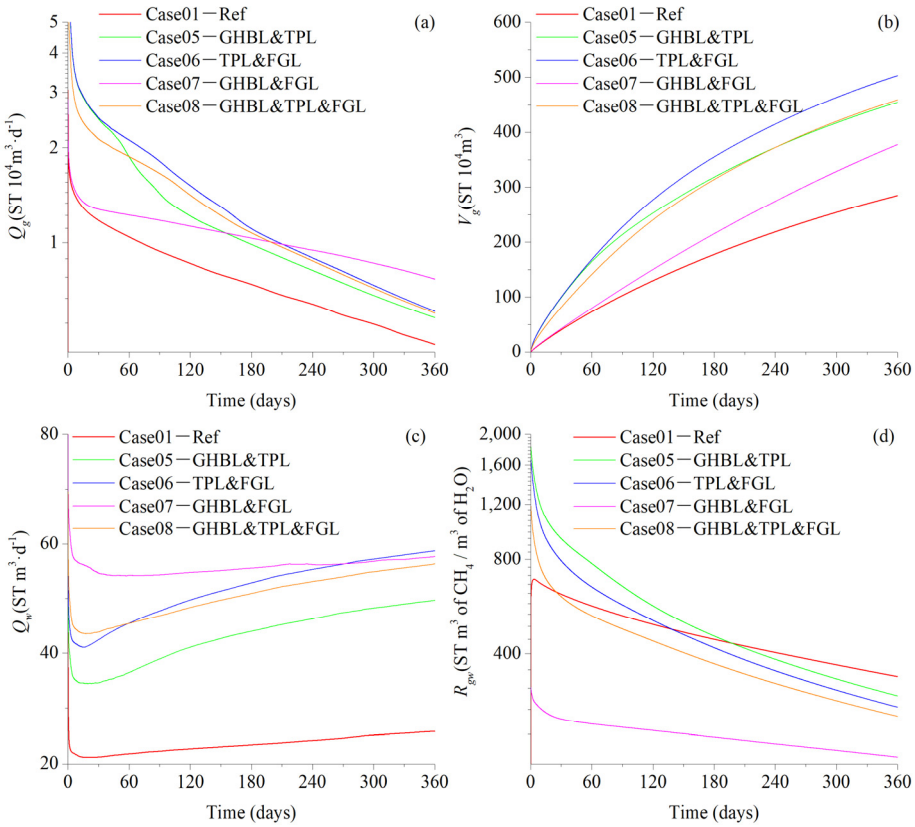

Figure 8. Gas and water production performances of multi-layer deployment of radial laterals: (**a**) Gas production rate Q_g. (**b**) cumulative gas production V_g. (**c**) Water production rate Q_w. (**d**) gas to water ratio R_{gw}.

Table 4. Productivity of multi-layer deployment of radial laterals.

Case	Deployment Location	Wellbore Contact Area (m^2)	Average Q_g (10^4 m^3/d)	V_g (10^4 m^3)	Compared to the Reference Case
Case 06	TPL & FGL	91.10	1.40	503.30	176.66%
Case 08	GHBL & TPL & FGL	91.10	1.28	459.00	161.11%
Case 05	GHBL & TPL	91.10	1.26	454.50	159.53%
Case 07	GHBL & FGL	91.10	1.05	377.60	132.54%
Case 01 (reference case)	-	43.98	0.79	284.90	100.00%

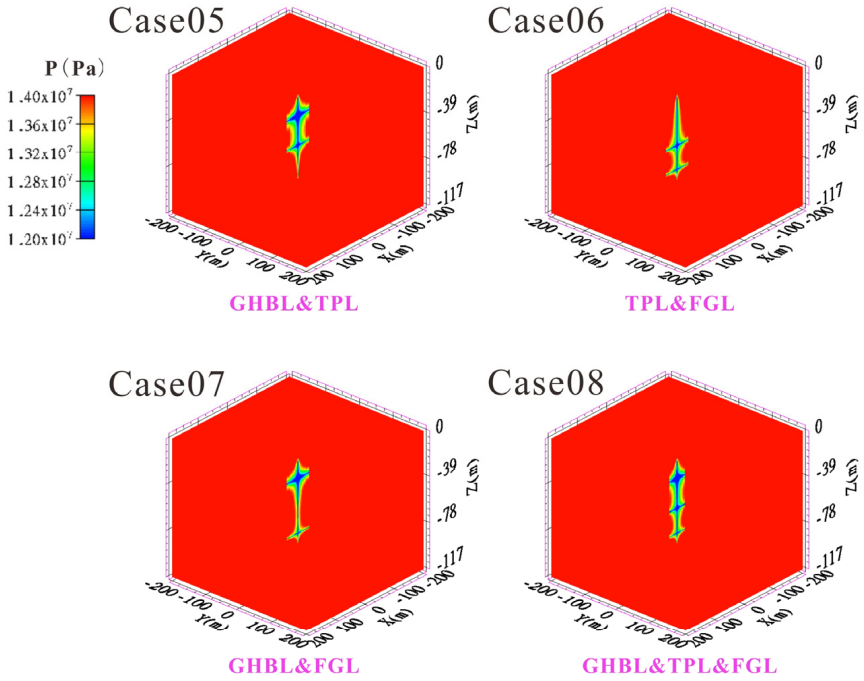

(a)

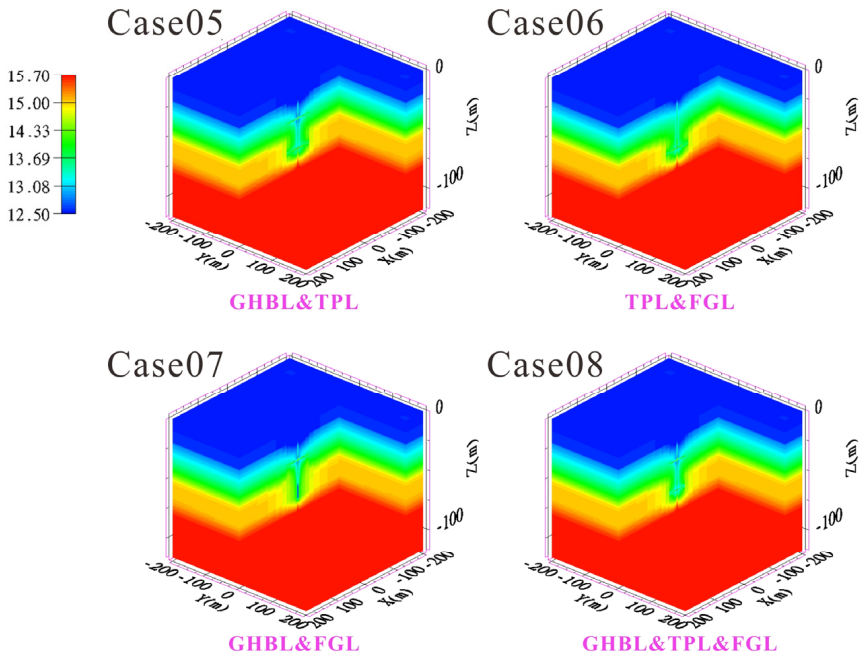

(b)

Figure 9. *Cont*.

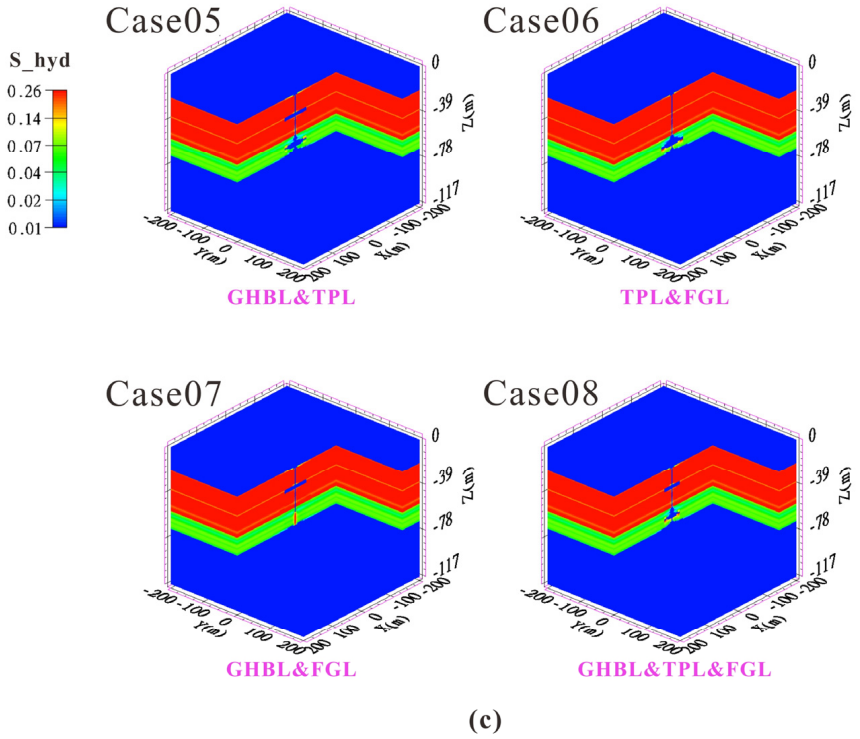

(c)

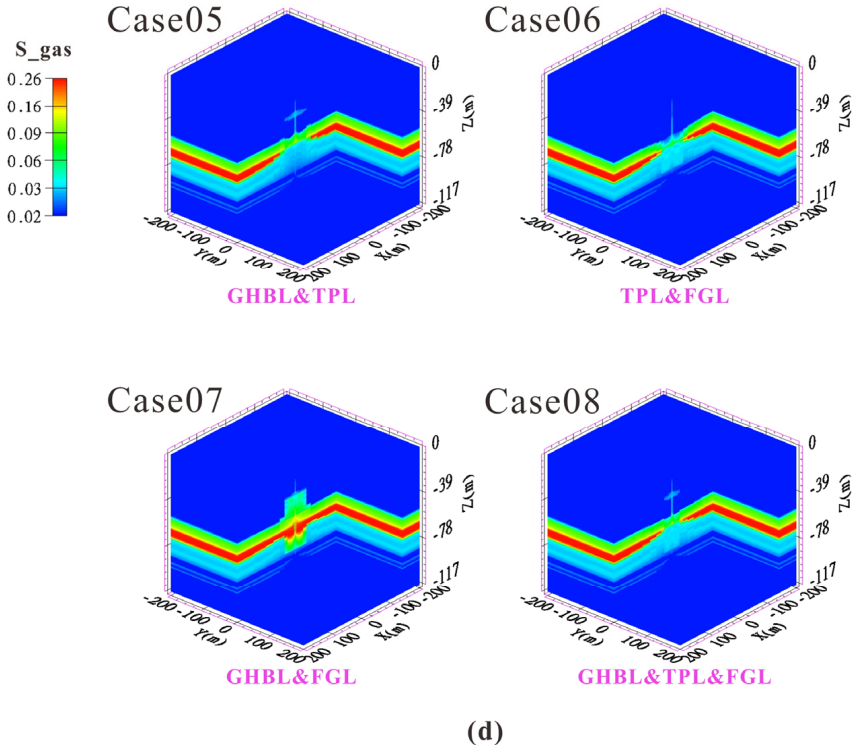

(d)

Figure 9. Spatial distribution diagram of pressure, temperature, and saturation of multi-layer deployment of radial laterals: (**a**) Pressure. (**b**) Temperature. (**c**) Hydrate saturation. (**d**) Gas saturation.

4.3. Comparisons of Production Performances

In general, the average Q_g and average R_{gw} are the two most direct indicators for evaluating the yield-increasing effect. The average Q_g and average R_{gw} of different radial-lateral deployment schemes during the 360-day production period are shown in Figure 10.

Obviously, under the same completion length and production pressure difference, when the radial laterals are deployed in the TPL, both the average Q_g and the average R_{gw} have the best performance. Therefore, it is recommended to use RJD technology to construct radial laterals in vertical wells for production enhancement, and the optimal deployment layer for radial laterals is the TPL. In addition, the production capacity of the above single vertical well is far below the standard for commercial exploitation of marine hydrates, which means that it is difficult to achieve commercial exploitation solely with a single well. The production mode of a "well factory" composed of clusters of vertical wells will receive more attention. Using RJD technology to construct radial laterals in vertical wells for production enhancement is feasible both theoretically and technically and is worthy of further research as a comprehensive topic.

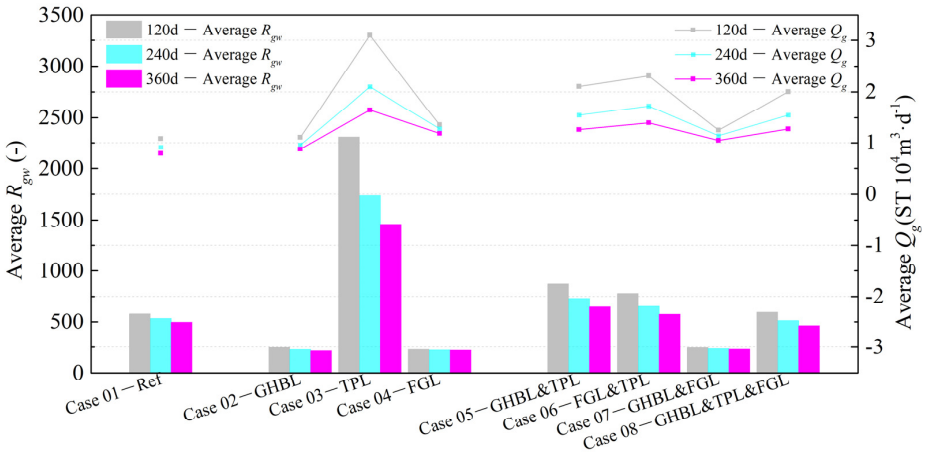

Figure 10. Histogram of average Q_g and average R_{gw} for different deployments of radial laterals; t = 120, 240, 360 days.

5. Conclusions

Based on the data of the first NGH field trial in the Shenhu Sea area, the gas production capability of Class 1-type hydrate reservoirs was numerically evaluated by vertical well depressurization with different radial-lateral deployment schemes, which provide a reference for NGH production. The following results were obtained: using RJD technology to construct radial laterals in vertical wells can effectively improve single-well productivity. The completion length of the radial laterals is 150 m with a radius of 0.05 m, and the production pressure difference is set to 6 MPa; when it is deployed at the TPL, it has the best gas and water production performance. After 360 days of production, its cumulative gas production V_g reaches 594.10 × 10^4 ST m^3, which is about twice that of single vertical well production. The above well schemes cannot meet the commercial development standards for NGHs offshore. Therefore, further research is needed to apply RJD technology to construct radial laterals to increase production capacity in the "well factory" production mode using vertical wells as the base well.

Author Contributions: T.W.: Conceptualization, Methodology, Software, Writing—Original Draft. M.Y.: Writing—review & editing, Supervision. H.L.: Funding acquisition. Z.C.: Formal analysis, Investigation. Z.L.: Formal analysis, Investigation. L.T.: Resources. K.L.: Data curation, Visualization. N.H.: Data curation, Visualization. J.W.: Supervision, Project administration. All authors have read and agreed to the published version of the manuscript.

Funding: This study was funded by the Guangdong Basic and Applied Basic Research Foundation (No. 2022A1515011902) and Guangzhou Science and Technology Program (No. 202206050002).

Data Availability Statement: The data presented in this study are available on request from the corresponding author.

Conflicts of Interest: Author Tinghui Wan was employed by the Guangzhou Marine Geological Survey. The remaining authors declare that the research was conducted in the absence of any commercial or financial relationships that could be construed as potential conflicts of interest.

Nomenclature

Symbols

L	open hole completion length (m)
n	quantity of lateral
l	lateral length (m)
x, y, z	cartesian coordinates (m)
Q_g	gas production rates at well (m^3/d)
Q_w	water production rates at well (m^3/d)
V_g	cumulative gas production at well (m^3/d)
R_{gw}	ratio of cumulative gas to cumulative gas (ST m^3 of CH_4/m^3 of H_2O)
M^κ	mass accumulation of component κ, (kg/m^3)
F^κ	mass flux of component κ, $kg/(m^2 \cdot s)$
q^κ	sink/source of component κ, $kg/(m^3 \cdot s)$
M^θ	energy accumulation (J/m^3)
F^θ	energy flux, $J/(m^2 \cdot s)$
q^θ	sink/source of heat, $J/(m^3 \cdot s)$
V	volume (m^3)
Γ	surface area (m^2)
t	times (s)
φ	porosity
S_β	saturation of phase β
ρ_β	density of phase β
X_β^κ	mass fraction of component κ in phase β
k	permeability (m^2)
$k_{r\beta}$	relative permeability of phase β
$\mu_{r\beta}$	viscosity of phase β, (Pa·s)
P_β	pressure of phase β, (Pa)
g	gravity acceleration (m/s^2)
b	Klinkenberg factor (Pa)
τ_β	medium tortuosity of phase β
D_β^κ	molecular diffusion coefficient of component κ in phase β, (m^2/s)
ρ_R	density of rock grain (kg/m^3)
C_R	specific heat of rock grain, $J/(kg \cdot ^\circ C)$
T	temperature (°C)
U_β	internal energy of phase β, (J/kg)
λ	average thermal conductivity, $W/(m \cdot K)$
h_β	specific enthalpy of phase β, (J/kg)
J_β^κ	mass diffusion of component κ in phase β, $kg/(m^2 \cdot s)$
ρ_H	hydrate density, (kg/m^3)
S_H	hydrate saturation
∇U_H	specific enthalpy of hydrate dissociation/formation, J/kg
Q_H	mass change of hydrate component under kinetic dissociation, kg
N_H	hydration number
∇	gradient operator
β	phase, $\beta = A, G, H, I$ is aqueous, gas, hydrate and ice, respectively
κ	component, $\kappa = w, m, i, h$ is water, methane, salt, and hydrate, respectively
T	phase equilibrium temperature (K)
e_1	regression parameter
e_2	regression parameter

Abbreviations

OB	overburden layer
UB	underburden layer
GHBL	gas hydrate-bearing layer
TPL	Three-phase layer
FGL	free gas layer
NGH	natural gas hydrate
RJD	Radial jet drilling

Symbols

φ_a	available porosity for fluids
φ_{rr}	relative magnitude of φ
S_s	solid saturation
F_{PT}	porosity adjustment factor
α_P	pore compressibility expansivity
α_T	pore thermal expansivity
P_{cap}	capillary pressure (Pa)
P_0	entry pressure of capillary pressure model (Pa)
S^*	saturation for capillary pressure model
S_{mxA}	maximum reference aqueous saturation of capillary
S_{irA}	irreducible saturation of aqueous phase
S_{irG}	irreducible saturation of gas phase
n_A	permeability reduction exponent for aqueous phase
n_G	permeability reduction exponent for gas phase
λ	parameter of capillary pressure model

Abbreviations

References

1. Sloan, E.D. Fundamental principles and applications of natural gas hydrates. *Nature* **2003**, *426*, 353–359. [CrossRef]
2. Boswell, R. Is gas hydrate energy within reach? *Science* **2009**, *325*, 957–958. [CrossRef]
3. Chong, Z.R.; Yang, S.H.B.; Babu, P.; Linga, P.; Li, X.S. Review of natural gas hydrates as an energy resource: Prospects and challenges. *Appl. Energy* **2016**, *162*, 1633–1652. [CrossRef]
4. Boswell, R.; Collett, T.S. Current perspectives on gas hydrate resources. *Energy Environ. Sci.* **2011**, *4*, 1206–1215. [CrossRef]
5. Yamamoto, K.; Terao, Y.; Fujii, T.; Ikawa, T.; Seki, M.; Matsuzawa, M.; Kanno, T. Operational Overview of the First Offshore Production Test of Methane Hydrates in the Eastern Nankai Trough. In Proceedings of the Offshore Technology Conference, Houston, TX, USA, 7 May 2014.
6. Yamamoto, K.; Wang, X.X.; Tamaki, M.; Suzuki, K. The second offshore production of methane hydrate in the Nankai Trough and gas production behavior from a heterogeneous methane hydrate reservoir. *RSC Adv.* **2019**, *9*, 25987–26013. [CrossRef]
7. Li, J.F.; Ye, J.L.; Qin, X.W.; Qiu, H.J.; Wu, N.Y.; Lu, H.L.; Xie, W.W.; Lu, J.A.; Peng, F.; Xu, Z.Q.; et al. The first offshore natural gas hydrate production test in South China Sea. *China Geol.* **2018**, *1*, 5–16. [CrossRef]
8. Ye, J.L.; Qin, X.W.; Xie, W.W.; Lu, H.L.; Ma, B.J.; Qiu, H.J.; Liang, J.Q.; Lu, J.A.; Kuang, Z.G.; Lu, C.; et al. The second natural gas hydrate production test in the South China Sea. *China Geol.* **2020**, *3*, 197–209. [CrossRef]
9. Cinelli, S.D.; Kamel, A.H. Novel technique to drill horizontal laterals revitalizes aging field. In Proceedings of the SPE/IADC Drilling Conference and Exhibition, Amsterdam, The Netherlands, 5–7 March 2013.
10. Mahmood, M.N.; Guo, B. Productivity comparison of radial lateral wells and horizontal snake wells applied to marine gas hydrate reservoir development. *Petroleum* **2021**, *7*, 407–413. [CrossRef]
11. Kamel, A.H. Radial Jet Drilling: A Technical Review. In Proceedings of the SPE Middle East Oil & Gas Show and Conference, Manama, Kingdom of Bahrain, 8 March 2017.
12. Kamel, A.H. A technical review of radial jet drilling. *J. Pet. Gas Eng.* **2017**, *8*, 79–89.
13. Huang, Z.; Huang, Z.W. Review of Radial Jet Drilling and the key issues to be applied in new geo-energy exploitation. *Energy Procedia* **2019**, *158*, 5969–5974. [CrossRef]
14. Li, G.S.; Tian, S.C.; Zhang, Y.Q. Research progress on key technologies of natural gas hydrate exploitation by cavitation jet drilling of radial wells. *Pet. Sci. Bulletin* **2020**, *5*, 349–365.
15. Zhang, P.P.; Tian, S.C.; Zhang, Y.Q.; Li, G.S.; Zhang, W.H.; Khan, W.A.; Ma, L.Y. Numerical simulation of gas recovery from natural gas hydrate using multi-branch wells: A three-dimensional model. *Energy* **2020**, *220*, 119549. [CrossRef]
16. Zhang, P.P.; Tian, S.C.; Zhang, Y.Q.; Li, G.S.; Wu, X.Y.; Wang, Y.H. Production simulation of natural gas hydrate using radial well depressurization. *Pet. Sci. Bull.* **2021**, *3*, 417–428.
17. Zhang, Y.Q.; Wu, X.Y.; Hu, X.; Zhang, B.; Lu, J.S.; Zhang, P.P.; Li, G.S.; Tian, S.C.; Li, X.M. Visualization and investigation of the erosion process for natural gas hydrate using water jet through experiments and simulation. *Energy Rep.* **2022**, *8*, 202–216. [CrossRef]
18. Zhang, P.P.; Zhang, Y.Q.; Wang, W.; Wang, T.Y.; Tian, S.C. Experimental study on natural gas hydrate extraction with radial well depressurization. *Pet. Sci. Bull.* **2022**, *03*, 382–393.
19. Hui, C.Y.; Zhang, Y.Q.; Zhang, P.P.; Wu, X.Y.; Huang, H.C.; Li, G.S. A study of natural gas hydrate reservoir stimulation by combining radial well fracturing and depressurization. In Proceedings of the ARMA US Rock Mechanics/Geomechanics Symposium, Santa Fe, NM, USA, 26–29 June 2022.
20. Hui, C.Y.; Zhang, Y.Q.; Zhang, P.P.; Wu, X.Y.; Li, G.S.; Huang, H.C. Numerical simulation of natural gas hydrate productivity based on radial well fracturing combined with the depressurization method. *Nat. Gas Ind.* **2022**, *42*, 152–164.
21. Li, G.S.; Huang, Z.W.; Li, J.B. Study of radial jet drilling key issues. *Pet. Drill. Tech.* **2017**, *45*, 1–9.

22. Yang, D.; Gao, Q.Y.; Zhu, Y.J.; Zhang, X.Q.; Zheng, B.D.; Wu, X.C. Research and application of radial hydraulic jet drilling technology in oil and gas wells. *Well Test.* **2017**, *26*, 67–69.
23. Song, X.Z.; Shi, Y.; Li, G.S.; Yang, R.Y.; Wang, G.S.; Zheng, R.; Li, J.C.; Lyu, Z.H. Numerical simulation of heat extraction performance in enhanced geothermal system with multilateral wells. *Appl. Energy* **2018**, *218*, 325–337. [CrossRef]
24. Zhang, W.; Liang, J.Q.; Lu, J.A.; Wei, J.G.; Su, P.B.; Fang, Y.X.; Guo, Y.Q.; Yang, S.X.; Zang, G.X. Accumulation features and mechanisms of high saturation natural gas hydrate in shenhu area, northern south china sea. *Pet. Explor. Dev.* **2017**, *44*, 708–719. [CrossRef]
25. Moridis, G.J.; Kowalsky, M.B.; Pruess, K. *TOUGH+ Hydrate V1.0 User's Manual*; Report LBNL-0149E; Lawrence Berkeley National Laboratory: Berkeley, CA, USA, 2008.
26. Su, Z.; Moridis, G.J.; Zhang, K.N.; Wu, N.Y. A huff-and-puff production of gas hydrate deposits in Shenhu area of South China Sea through a vertical well. *J. Pet. Sci. Eng.* **2012**, *86–87*, 54–61. [CrossRef]
27. Yin, Z.Y.; Moridis, G.J.; Chong, Z.R.; Linga, P. Effectiveness of multi-stage cooling processes in improving the CH4-hydrate saturation uniformity in sandy laboratory samples. *Appl. Energy* **2019**, *250*, 729–747. [CrossRef]
28. Zhang, K.N.; Moridis, G.J.; Wu, Y.S.; Pruess, K. A domain decompositionapproach for large-scale simulations of flow processes in hydrate-bearing geologic media. In Proceedings of the 6th International Conference on Gas Hydrates, Vancouver, BC, Canada, 6–10 July 2008; ICGH: Vancouver, BC, Canada, 2009.
29. Kowalsky, M.B.; Moridis, G.J. Comparison of kinetic and equilibrium reaction models in simulating gas hydrate behavior in porous media. *Energy Convers. Manag.* **2007**, *48*, 1850–1863. [CrossRef]
30. Li, G.; Li, X.S.; Zhang, K.N.; Li, B.; Zhang, Y. Effects of Impermeable Boundaries on Gas Production from Hydrate Accumulations in the Shenhu Area of the South China Sea. *Energies* **2013**, *6*, 4078–4096. [CrossRef]
31. Yu, T.; Guan, G.Q.; Wang, D.Y.; Song, Y.C.; Abudula, A. Numerical investigation on the long-term gas production behavior at the 2017 Shenhu methane hydrate production-site. *Appl. Energy* **2021**, *285*, 116466. [CrossRef]
32. Sun, J.X.; Zhang, L.; Ning, F.L.; Lei, H.W.; Liu, T.L.; Hu, G.W.; Lu, H.L.; Lu, J.A.; Liu, C.L.; Jiang, G.S.; et al. Production potential and stability of hydrate-bearing sediments at the site GMGS3-W19 in the South China Sea: A preliminary feasibility study. *Mar. Pet. Geol.* **2017**, *86*, 447–473. [CrossRef]
33. Yuan, Y.L.; Xu, T.F.; Xin, X.X.; Xia, Y.L. Multiphase Flow Behavior of Layered Methane Hydrate Reservoir Induced by Gas Production. *Geofluids* **2017**, *2017*, 1–15. [CrossRef]
34. Sun, J.X.; Ning, F.L.; Li, S.; Zhang, K.; Liu, T.L.; Zhang, L.; Jiang, G.S.; Wu, N.Y. Numerical simulation of gas production from hydrate-bearing sediments in the Shenhu area by depressurising: The effect of burden permeability. *J. Unconv. Oil Gas Resour.* **2015**, *12*, 23–33. [CrossRef]
35. Feng, Y.C.; Chen, L.; Suzuki, A.; Kogawa, T.; Okajima, J.; Komiya, A.; Maruyama, S. Enhancement of gas production from methane hydrate reservoirs by the combination of hydraulic fracturing and depressurization method. *Energy Convers. Manag.* **2019**, *184*, 194–204. [CrossRef]
36. Moridis, G.J.; Reagan, M.T.; Kim, S.J.; Seol, Y.; Zhang, K. Evaluation of the Gas Production Potential of Marine Hydrate Deposits in the Ulleung Basin of the Korean East Sea. *SPE J.* **2007**, *14*, 759–781. [CrossRef]
37. Sun, Y.H.; Ma, X.L.; Guo, W.; Jia, R.; Li, B. Numerical simulation of the short- and long-term production behavior of the first offshore gas hydrate production test in the South China Sea. *J. Pet. Sci. Eng.* **2019**, *181*, 106196. [CrossRef]
38. Ma, X.L.; Sun, Y.H.; Liu, B.C.; Guo, W.; Jia, R.; Li, B.; Li, S.L. Numerical study of depressurization and hot water injection for gas hydrate production in China's first offshore test site. *J. Pet. Sci. Eng.* **2020**, *83*, 103530. [CrossRef]
39. Cao, X.X.; Sun, J.X.; Qin, F.F.; Ning, F.L.; Mao, P.X.; Gu, Y.H.; Li, Y.L.; Zhang, H.; Yu, Y.J.; Wu, N.Y. Numerical analysis on gas production performance by using a multilateral well system at the first offshore hydrate production test site in the Shenhu area. *Energy* **2023**, *270*, 126690. [CrossRef]
40. Qin, X.W.; Liang, Q.Y.; Ye, J.L.; Yang, L.; Qiu, H.J.; Xie, W.W.; Liang, J.Q.; Lu, J.A.; Lu, C.; Lu, H.L.; et al. The response of temperature and pressure of hydrate reservoirs in the first gas hydrate production test in South China Sea. *Appl. Energy* **2020**, *278*, 115649. [CrossRef]